Enhancing Taiji's parameter estimation under nonstationarity: A time-frequency domain framework for Galactic binaries and instrumental noises

Minghui Du,[1,*] Ziren Luo,[1,2,3] and Peng Xu[1,2,3,4,†]

[1]*Center for Gravitational Wave Experiment, National Microgravity Laboratory, Institute of Mechanics, Chinese Academy of Sciences, Beijing 100190, China*
[2]*Taiji Laboratory for Gravitational Wave Universe (Beijing/Hangzhou), University of Chinese Academy of Sciences (UCAS), Beijing 100049, China*
[3]*Key Laboratory of Gravitational Wave Precision Measurement of Zhejiang Province, Hangzhou Institute for Advanced Study, UCAS, Hangzhou, 310024, China*
[4]*Lanzhou Center of Theoretical Physics, Lanzhou University, Lanzhou 730000, China*

(Received 27 June 2025; accepted 23 September 2025; published 17 October 2025)

The data analysis of space-based gravitational wave detectors like Taiji faces significant challenges from nonstationary noise, which compromises the efficacy of traditional frequency-domain analysis. This work proposes a unified framework based on short-time Fourier transform (STFT) to enhance parameter estimation of Galactic binary and characterization of instrumental noise under nonstationarity. Segmenting data into locally stationary intervals, we derive STFT-based models for signals and noises, and implement Bayesian inference via the extended Whittle likelihood. Validated through the analysis of verification Galactic binaries and instrumental noises, our STFT approach outperforms frequency-domain methods by reducing the uncertainty and bias of estimation, successfully recovering low signal-to-noise ratio signals missed by frequency-domain analysis, and mitigating the degeneracy among noise parameters. The framework's robustness against noise drifts and computational efficiency highlight its potential for integration into future global analysis pipelines.

DOI: 10.1103/gpmh-1hqx

I. INTRODUCTION

In the upcoming decade, space-based gravitational wave (GW) detectors, including the Laser Interferometer Space Antenna (LISA) [1,2], Taiji [3–5] and Tianqin [6], will expand our exploration of GW universe to the 0.1 mHz–Hz band by detecting a rich spectrum of sources, such as massive black hole binaries (MBHBs) [7–9], Galactic binaries (GBs, mostly double white dwarfs) [10–13], extreme mass-ratio inspirals (EMRIs) [14], stellar-mass black hole binaries (sBHBs) [15,16], as well as stochastic GW backgrounds (SGWBs) of astrophysical and cosmological origins [17,18]. Deriving scientific implications from these detections hinges critically on advanced data analysis methods. In this paper, we intend to address one of the key challenges faced by Taiji's data analysis [19], that is the problem caused by nonstationary noise. In principle, the proposed methodology also applies to LISA and Tianqin due to similar mission concepts.

Different from current observations of LIGO-Virgo-KAGRA, the majority of detectable signals in the space-based band are continuous GWs. For instance, due to their quasimonochromatic nature, GBs' observational timescales are expected to be years. Observing GBs via GWs offers distinct advantages, as GWs are almost "transparent" to interstellar gas, dust, and other stars in the Galaxy [20]. Therefore, inferring the properties of GBs provides ideal probes for the structure and evolution of the Milky Way [21]. Another key motivation for precise estimation of GB parameters stems from the signal-dominated characteristics of Taiji's data. With approximately $\mathcal{O}(10^4)$ resolvable and $\mathcal{O}(10^7)$ unresolved GB signals overlapping in the data stream [22,23], it is necessary to perform so-called "global fit" analysis to simultaneously model all the signals and noise components [24–27]. In other words, inaccurate estimation and subtraction of a single signal could potentially compromise the subsequent analysis.

On the other hand, characterizing instrumental noises also typically relies on accumulating long-duration data [28,29]. Accurate knowledge of instrumental noises is essential for both the statistical inference of resolvable signals [30,31] and the detection of SGWB [32]. Besides, it also serves as an important indicator for the detector's in-orbit performance. Accurate and timely evaluation of noises would enable rapid responses to any potential

*Contact author: duminghui@imech.ac.cn
†Contact author: xupeng@imech.ac.cn

changes by the mission's ground segment. Under the signal-dominated scenario, joint estimation of noise and SGWB parameters has been demonstrated in previous studies (e.g., Refs. [28,29,33–36]), while a comprehensive global analysis of resolvable signals, SGWBs, and instrumental noises still remains to be established. A a way around this difficulty is to utilize the "null" time-delay interferometry (TDI) channels. To mitigate the overwhelming laser frequency noise, data transmitted to Earth must undergo TDI processing prior to the scientific analysis [37]. Among all the divergent schemes of TDI combinations, "null" channels, such as the Michelson-T and Sagnac ζ channels [38–41] are particular valuable since they are insensitive to GWs, offering a direct approach to understand instrumental noises.

When extracting information from long-duration data, the statistical properties of noise inevitably change over time, posing challenges for data analysis. The nonstationarity can be attributed to multiple mechanisms [42], including the cyclostationary astrophysical foreground caused by the anisotropic distribution of unresolvable GBs [45–47], the variations in payloads, spacecraft (S/C) platforms and in-orbit environments (as demonstrated by LISA Pathfinder [48–50]), etc. Additionally, the noise transfer functions of certain TDI combinations, especially the Michelson-T channel used for noise characterization [51,52], are sensitive to the variation of armlengths (which are used as the "delays"), introducing further nonstationarity to the resulting TDI data. Naturally, these effects necessitate regular characterization and updating of the noise models, or otherwise they will lead to bias in parameter estimation or incorrect confidence intervals. More critically, nonstationarity would undermine the efficacy of conventional frequency-domain analysis methods. Nonstationarity violates the fundamental assumptions of the Whittle likelihood framework [53], as the frequency-domain noise covariance matrix becomes nondiagonal [47,54]. Consequently, calculating the likelihood function would require accounting for the off-diagonal elements, substantially increasing computational costs of Bayesian inference.

A theoretically viable approach to addressing these problems is to transition the whole statistical analysis framework to the time-frequency domain. After Ref. [55] provided a concise and systematic overview of time-frequency GW data analysis based on the Wilson-Daubechies-Meyer wavelet, Ref. [56] applied this framework to the characterization of the time-varying GB foreground, and reevaluated the delectabilities of LISA to GBs and MBHBs. Another application to the estimation of LISA-band sBHB was presented in Ref. [57], showing that this framework allows for transient glitches in the data. Reference [58] proposed another approach to deal with the noise nonstationarity and data gap, which was built on $\mathcal{F}$ statistics and the short-time Fourier transform (STFT). As examples, the paper assessed its future applicability in the early warning of binary neutron stars (BNSs) (for third-generation ground-based detectors) and MBHB (for LISA) in terms of a "relative error" metric. Also for third-generation ground-based detectors, Ref. [59] investigated the impact of nonstationary noise on the accuracy of BNS parameter estimation, and proposed a robust treatment by normalizing noise power spectral density (PSD) along the signal's time-frequency track. In a broader sense, time-frequency representations are widely adopted in template-free approaches such as coherent wave burst [60].

Given the potential advantages of time-frequency analysis in space-based detections, and considering its applications in other long-duration data analysis tasks remain to be fully explored, in this paper, we develop a STFT-based Bayesian analysis framework to enhance Taiji's (also LISA/Tianqin's) estimation of GB and instrumental noise parameters in the presence of nonstationarity. Specifically, a STFT template for the TDI response of GB signal, and a time-varying noise spectral model are derived. Further, under the local stationarity condition, we extend the key statistics such as inner product and Whittle likelihood to the time-frequency domain. The computation of aforementioned models and likelihood can be simply accelerated on GPUs using CUPY, highlighting their potential to be integrated into future global fit analyses. When tested on the estimation of verification GB (VGB) [61] parameters, our STFT approach achieves higher accuracy and reduced bias compared to the conventional frequency-domain method. For the estimation of noise parameters, we demonstrate our framework on the time-varying T channel (driven by armlength variation) as an example. The results show that time-frequency analysis not only establishes a more rigorous theoretical foundation, but also relieves the degeneracies among parameters through explicit modeling of temporal features. It should be noted that this idea has broader applicability: one may leverage the modeled temporal features to distinguish anisotropic stochastic signals from noises, as demonstrated in Ref. [62].

The outline of this paper is as follows: Sec. II establishes the theoretical formalism of our STFT-based framework, including the models of GB signals and instrumental noises, as well as the extended Bayesian statistics. Section III validates the framework on VGB parameter estimation, and demonstrates its advantage over conventional frequency-domain analysis under noise nonstationarity. Another data analysis task is illustrated in Sec. IV, where we apply the STFT framework to instrumental noise characterization via the Michelson T channel, showing how explicit modeling of time-dependence mitigates parameter degeneracies. Conclusions and outlooks for future works are provided in Sec. V. Details of the window function and the full posterior distributions of representative VGBs are presented in Appendices A and B, respectively.

Throughout this paper, we assume all the data are perfectly synchronized to barycentric coordinate time,

and the laser noise, clock noise, S/C jitter, and tilt-to-length noise have been sufficiently mitigated during or after TDI processing, hence they are excluded from our study. The time spans of all simulations are set to 1 year.

II. STFT FRAMEWORK FOR GW SIGNAL ESTIMATION AND NOISE CHARACTERIZATION

A. The time-domain signal and noise models of Taiji

Despite the extensive literature describing Taiji and LISA's GW responses and noise budgets, a systematic introduction would still be necessary for subsequent analyses. We start from the "single-arm" Doppler measurement denoted as $\eta_{ij}(t)$, which is essentially the combination of several raw interferometor readouts [63–66]. Generally, η_{ij} is the superposition of single-arm GW responses $y_{ij}(t)$ and instrumental noises $n_{ij}(t)$,

$$\eta_{ij}(t) = y_{ij}(t) + n_{ij}(t), \tag{1}$$

where $ij \in \mathcal{I}_2 \equiv \{12, 23, 31, 21, 32, 13\}$, i, and j specifying the index of S/C receiving and emitting lasers, respectively. $y_{ij}(t)$ can be formulated as [67–69]

$$\begin{aligned} y_{ij}(t) &\equiv \frac{\nu_{\text{receive}} - \nu_{\text{send}}}{\nu_{\text{send}}} \\ &\approx \frac{1}{2(1-\hat{\boldsymbol{k}}\cdot\hat{\boldsymbol{n}}_{ij}(t))}\left[H_{ij}\left(t - d_{ij}(t) - \frac{\hat{\boldsymbol{k}}\cdot\boldsymbol{R}_j(t)}{c}\right)\right. \\ &\quad \left. - H_{ij}\left(t - \frac{\hat{\boldsymbol{k}}\cdot\boldsymbol{R}_i(t)}{c}\right)\right]. \end{aligned} \tag{2}$$

$\boldsymbol{R}_i(t)$ denotes the position of S/C$_i$ in the Solar system barycenter (SSB) frame, $d_{ij}(t)$ is the light travel time from S/C$_j$ to S/C$_i$ (t being the time of reception), and $\hat{\boldsymbol{n}}_{ij}(t)$ is the unit vector along this arm. During realistic detection, these quantities should be derived via orbit determination and inter-S/C ranging [70,71], and they generally deviate from the idealistic equal-arm orbit models as adopted by LISA data challenge (LDC) [68]. To incorporate more realistic orbital dynamics, all the models and simulations of this work utilize the numerically simulated Taiji Data Challenge orbit [19]. The projection of GW tensor on arm ij reads

$$H_{ij}(t) \equiv h_+(t)\zeta_{+,ij}(t) + h_\times(t)\zeta_{\times,ij}(t), \tag{3}$$

where

$$\zeta_{+,ij}(t) = \cos(2\psi)\xi_{+,ij}(t) + \sin(2\psi)\xi_{\times,ij}(t), \tag{4}$$

$$\zeta_{\times,ij}(t) = -\sin(2\psi)\xi_{+,ij}(t) + \cos(2\psi)\xi_{\times,ij}(t), \tag{5}$$

$$\xi_{+,ij}(t) = [\hat{\boldsymbol{n}}_{ij}(t)\cdot\hat{\boldsymbol{u}}]^2 - [\hat{\boldsymbol{n}}_{ij}(t)\cdot\hat{\boldsymbol{v}}]^2, \tag{6}$$

$$\xi_{\times,ij}(t) = 2[\hat{\boldsymbol{n}}_{ij}(t)\cdot\hat{\boldsymbol{u}}][\hat{\boldsymbol{n}}_{ij}(t)\cdot\hat{\boldsymbol{v}}]. \tag{7}$$

The ζs and ξs are the antenna pattern functions in the source frame and SSB frame, respectively, and ψ stands for the polarization angle. For a GW source located at Ecliptic longitude λ and Ecliptic latitude β, the Cartesian coordinate components of unit vectors $\hat{\boldsymbol{u}}$, $\hat{\boldsymbol{v}}$, and $\hat{\boldsymbol{k}}$ are

$$\hat{\boldsymbol{u}} = [\sin\lambda, -\cos\lambda, 0], \tag{8}$$

$$\hat{\boldsymbol{v}} = [-\sin\beta\cos\lambda, -\sin\beta\sin\lambda, \cos\beta], \tag{9}$$

$$\hat{\boldsymbol{k}} = -[\cos\beta\cos\lambda, \cos\beta\sin\lambda, \sin\beta]. \tag{10}$$

To model the waveform of GB, we utilize the Newtonian approximation and expand the phase of GW to the third power of time, consistent with the widely adopted form in the literature (e.g., Ref. [67]),

$$h_+(t) = A(1+\cos^2\iota)\cos\varphi(t), \tag{11}$$

$$h_\times(t) = 2A\cos\iota\sin\varphi(t), \tag{12}$$

where the amplitude A and phase $\varphi(t)$ are related to the chirp mass $\mathcal{M}_c$, luminosity distance D, initial GW phase φ_0, initial GW frequency f_0, and its derivatives as

$$A = \frac{2(G\mathcal{M}_c)^{5/3}(\pi f_0)^{2/3}}{c^4 D}, \tag{13}$$

$$\varphi(t) = 2\pi\left(f_0 t + \frac{1}{2}\dot{f}_0 t^2 + \frac{1}{6}\ddot{f}_0 t^3\right) + \varphi_0, \tag{14}$$

respectively, with

$$\ddot{f}_0 = \frac{11}{3}\frac{\dot{f}_0^2}{f_0}. \tag{15}$$

In principle, the noise term $n_{ij}(t)$ of Eq. (1) should be regarded as the synthesis of multiple noises, such as test-mass acceleration noises, optical path noises, readout noises, and fiber backlink noises, etc. The dominant contributions can be described as a two-component model including the optical metrology system (OMS) noises N_{ij} and test-mass acceleration (ACC) noises δ_{ij},

$$n_{ij}(t) = N_{ij}(t) + \delta_{ij}(t) + \mathbf{D}_{ij}\delta_{ji}(t). \tag{16}$$

The delay operator $\mathbf{D}_{ij}$ is defined as $\mathbf{D}_{ij}f(t) \equiv f(t - d_{ij}(t))$, when acting on an arbitrary function of time $f(t)$. Readers may refer to Ref. [72] for a more comprehensive and up-to-date model incorporating other subdominant noise sources. According to the baseline design of Taiji, the "nominal" PSDs of N_{ij} and δ_{ij} take the forms of

$$S_{ij,\mathrm{OMS}}(f) = A^2_{ij,\mathrm{OMS}}\left(\frac{2\pi f}{c}\right)^2\left[1+\left(\frac{2\ \mathrm{mHz}}{f}\right)^4\right],$$
$$S_{ij,\mathrm{ACC}}(f) = A^2_{ij,\mathrm{ACC}}\left(\frac{1}{2\pi f c}\right)^2\left[1+\left(\frac{0.4\ \mathrm{mHz}}{f}\right)^2\right]\times\left[1+\left(\frac{f}{8\ \mathrm{mHz}}\right)^4\right], \quad (17)$$

where $A_{ij,\mathrm{OMS}} \equiv 8\times10^{-12}\ \mathrm{m}/\sqrt{\mathrm{Hz}}$ and $A_{ij,\mathrm{ACC}} \equiv 3\times10^{-15}\ \mathrm{m/s^2}/\sqrt{\mathrm{Hz}}$. The OMS and ACC noises dominate at the high and low frequencies, respectively. Notice that in realistic detection, we cannot expect these PSDs to be identical for all the ijs, and they are very likely to drift over time.

To effectively suppress laser frequency noise, Taiji utilizes the TDI observables rather than single-arm measurements for GW detection. Despite the variety of TDI configurations [73–75], all the TDI observables can be written in a unified form,

$$\mathrm{TDI} = \sum_{ij\in\mathcal{I}_2}\mathbf{P}_{ij}\eta_{ij}. \quad (18)$$

Taking the Michelson X_2 channel as an example, one has

$$\begin{aligned}
\mathbf{P}_{12} &= 1-\mathbf{D}_{131}-\mathbf{D}_{13121}+\mathbf{D}_{1213131},\\
\mathbf{P}_{23} &= 0,\\
\mathbf{P}_{31} &= -\mathbf{D}_{13}+\mathbf{D}_{1213}+\mathbf{D}_{121313}-\mathbf{D}_{13121213},\\
\mathbf{P}_{21} &= \mathbf{D}_{12}-\mathbf{D}_{1312}-\mathbf{D}_{131212}+\mathbf{D}_{12131312},\\
\mathbf{P}_{32} &= 0,\\
\mathbf{P}_{13} &= -1+\mathbf{D}_{121}+\mathbf{D}_{12131}-\mathbf{D}_{1312121},
\end{aligned} \quad (19)$$

where $\mathbf{D}_{i_1i_2i_3\ldots}f(t) \equiv \mathbf{D}_{i_1i_2}\mathbf{D}_{i_2i_3}\ldots f(t)$. The formulas of Y_2 and Z_2 channels can be obtained from the permutation rule $1\to2, 2\to3, 3\to1$. Further, the "signal" channel A_2, E_2 and the "null" channel T_2 are defined as [76]

$$A_2 = \frac{Z_2-X_2}{\sqrt{2}}, \quad (20)$$

$$E_2 = \frac{X_2-2Y_2+Z_2}{\sqrt{6}}, \quad (21)$$

$$T_2 = \frac{X_2+Y_2+Z_2}{\sqrt{3}}. \quad (22)$$

B. The STFT formalism for Bayesian inference

Time-frequency domain representations such as STFT [58] and wavelet decompositions [55] are generally more suitable than Fourier transform under nonstationary noises [77]. Meanwhile, data gaps are also inevitable for long-duration scientific operations, either due to scheduled maintenances or unscheduled disruptions. Recent studies [78,79] suggested that gaps in LISA data could occur up to hundreds of times per year, resulting in a duty cycle of ~80% or less [80]. To date, the gap profile of Taiji is still not fully characterized, while to also account for its potential impacts, we choose STFT among all time-frequency domain representations, since data is naturally divided into time segments in the presence of gaps.

When adopting STFT, a technical consideration follows, that is, each segment should be windowed to prevent spectral leakage. The windowing process also induces distortion of waveforms, therefore the template used in matched filtering must be identically windowed to ensure unbiased estimation. Following practices in ground-based detection and balancing spectral leakage suppression against signal strength preservation, we employ a Tukey window with parameter $\alpha = 0.1$. Its mathematical expressions in the time and frequency domains are detailed in Appendix A.

Consider a generic case where the data is divided into N_t segments, with the m-th segment centering at t_m and having a length of T_m. Before STFT, each segment is shifted to starting at $t=0$ and multiplied by a window function $w_m(t-T_m/2)$ [since the window is originally defined in $(-T_m/2, T_m/2)$]. Therefore, taking the TDI-X_2 channel as an example, the windowed STFT of the m-th segment is

$$\bar{X}_2(t_m,f) \equiv \int_0^{T_m}\mathrm{d}t\, e^{-i2\pi ft}w_m\left(t-\frac{T_m}{2}\right)\times X_2\left(t+t_m-\frac{T}{2}\right). \quad (23)$$

The derivation of STFT GB template generally leverages the fact that terms related to detector orbit and GW frequency are slowly varying, while the GW phase exhibits relatively fast variation [81]. Within current models for GB populations (e.g., Refs. [82,83]), the evolution of GW frequency is limited to $\dot{f}_0 \lesssim \mathcal{O}(10^{-12})$ Hz/s, thus we can safely approximate $\varphi(t)$ to the linear order during a time span of $\mathcal{O}(10^2)$ s [84], and write $y_{ij}(t)$ as

$$y_{ij}(t) \approx B_{y,ij}(t)e^{i\varphi(t)} + \mathrm{c.c.}, \quad (24)$$

where "c.c." stands for the complex conjugate of the first term, and

$$B_{y,ij}(t) \equiv -\frac{i}{2}\dot{\varphi}(t)d_{ij}\mathrm{sinc}\left[\frac{1}{2}\dot{\varphi}(t)d_{ij}(1-\hat{\boldsymbol{k}}\cdot\hat{\boldsymbol{n}}_{ij})\right]\times e^{-i\dot{\varphi}(t)\left[\frac{d_{ij}}{2}+\frac{\hat{\boldsymbol{k}}\cdot(\boldsymbol{p}_i+\boldsymbol{p}_j)}{2c}+\frac{\hat{\boldsymbol{k}}\cdot\boldsymbol{R}_0}{c}\right]}\left(\sum_\alpha\zeta_{\alpha,ij}A_\alpha\right), \quad (25)$$

where $\boldsymbol{R}_0$ is the center-of-mass of the S/Cs, $\boldsymbol{p}_i \equiv \boldsymbol{R}_i - \boldsymbol{R}_0$, and all the d_{ij}, $\hat{\boldsymbol{n}}_{ij}$, $\boldsymbol{p}_i$, and $\boldsymbol{R}_0$ take the values at t. $A_\alpha(\alpha\in\{+,\times\})$ are defined as

$$A_+ \equiv \frac{1}{2}A(1+\cos^2\iota), \qquad A_\times \equiv -iA\cos\iota. \tag{26}$$

Also due to the slow variation of GW frequency and detector orbit, each delay operation $\mathbf{D}f(t) \equiv f(t-d)$ in Eqs. (18) and (19) can be replaced by a factor of $e^{-i\dot{\varphi}(t)d}$, hence simplifying the modeling of TDI combination. Considering a typical maximum segment length of $\mathcal{O}(10^5)$ s, we further expand the "fast" term $\varphi(t)$ around the center of the segment, and neglect the quadratic term [corresponding to an error of less than $\mathcal{O}(10^{-2})$]. By analytically evaluating the integral in Eq. (23), the resulting GB template reads

$$\bar{X}_2(t_m,f) \approx e^{-i\pi fT}\tilde{w}_m\left[f-\frac{\dot{\varphi}(t_m)}{2\pi}\right]A_{X_2}(t_m) \tag{27}$$

for $f > 0$, where

$$\begin{aligned} A_{X_2}(t_m) = &\{(1-\Delta_{31}^2)[B_{y,12}(t_m)+\Delta_{12}B_{y,21}(t_m)] \\ &-(1-\Delta_{12}^2)[B_{y,13}(t_m)+\Delta_{31}B_{y,31}(t_m)]\} \\ &\times(1-\Delta_{12}^2\Delta_{31}^2)e^{i\varphi(t_m)}, \end{aligned} \tag{28}$$

with $\Delta_{ij} \equiv e^{-i\dot{\varphi}(t_m)d_{ij}(t_m)}$. Note that we do not distinguish between d_{ij} and d_{ji} since $f_0|d_{ij}-d_{ji}|$ is typically less than $\mathcal{O}(10^{-4})$ [87]. The templates for $\{Y_2, Z_2\}$ and $\{A_2, E_2, T_2\}$ channels can be obtained via the permutation rule and Eq. (20).

The deduction of the time-varying noise spectral model is relatively simpler. Assuming that N_{ij} and δ_{ij} for different laser links and test-masses do not correlate, the noise PSD of a general TDI observable reads

$$S(t,f) = \sum_{ij}[|\tilde{\mathbf{P}}_{ij}|^2 S_{ij,\mathrm{OMS}} + |\tilde{\mathbf{P}}_{ij}+\tilde{\mathbf{D}}_{ji}\tilde{\mathbf{P}}_{ji}|^2 S_{ij,\mathrm{ACC}}]. \tag{29}$$

Generally $\tilde{\mathbf{P}}_{ij}$, $S_{ij,\mathrm{OMS}}$, and $S_{ij,\mathrm{ACC}}$ all depend on t and f. The time dependence of $\tilde{\mathbf{P}}_{ij}$ originates from that of $\tilde{\mathbf{D}}_{ij}$, i.e.,

$$\tilde{\mathbf{D}}_{ij}(t,f) = e^{-i2\pi f d_{ij}(t)}. \tag{30}$$

To obtain $S(t,f)$ from data, the Fourier transform should be calculated over a time segment that is short enough for the noises to be considered stationary, and long enough to ensure the frequency resolution of signal and cover the sensitive band of Taiji.

Under the conditions of local stationarity and statistical independence among segments (as verified in Refs. [55,78]), all the time-frequency pixels are uncorrelated, thus we define the inner product between data d and template h as

$$\langle d|h\rangle \equiv 4\sum_{m=1}^{Nt}\sum_{n=1}^{N_{f,m}}\frac{1}{T_m}\frac{\Re[\bar{d}(t_m,f_n)\bar{h}^*(t_m,f_n)]}{S(t_m,f_n)}, \tag{31}$$

where N_{f_m}, defined as the integer part of $f_{\mathrm{sample}}/(2T_m)$, denotes the number of frequency-domain data points obtained from the Fourier transform of the m-th time segment, with f_{sample} standing for the sampling rate. The frequencies are given by $f_n = n/T_m$ for $n \in \{1,2,\ldots,N_{f_m}\}$, spanning from the frequency resolution $1/T_m$ to the largest integer multiple of $1/T_m$ not exceeding the Nyquist frequency $f_{\mathrm{sample}}/2$. Accordingly, the mismatch $\mathcal{MM}$, a metric quantifying the discrepancy between waveform h_1 and h_2, is also extended to STFT representation as

$$\mathcal{MM} = 1 - \frac{\langle h_1|h_2\rangle}{\sqrt{\langle h_1|h_1\rangle\langle h_2|h_2\rangle}}. \tag{32}$$

The validation of our STFT GB template is evaluated using this metric. To ensure the accuracy of templates used in the investigation of Sec. III, tests are conducted on the 55 VGBs collected by Ref. [61]. According to the model in Sec. II A, we simulate VGB signals in the time domain using the Taiji Data Challenge toolkit TRIANGLE-SIMULATOR [88], slice each of them into uniform segments, perform STFT, and then compare with the templates. By varying the lengths of segments, we calculate and compare the resulting mismatches in Fig. 1. Consistent with our derivation, for segment length of 1 day and 2.5 days ($\sim 10^5$ s), the mismatches are generally at $\mathcal{O}(10^{-3})$ or $\mathcal{O}(10^{-4})$, satisfying the requirement for unbiased estimation [89,90]. Also as expected, increasing the duration would compromise the accuracy of STFT templates. In practice, the selection of T_m should depend on both the locations of gaps and the variations of noises. Until further characterizations of Taiji's gap and nonstationary statistics are available, we currently take $T_m \equiv 2.5$ days as a representative example.

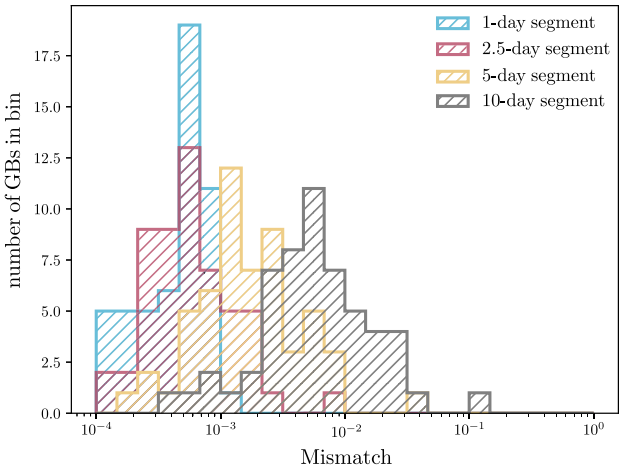

FIG. 1. Mismatches between STFT templates and rigorous time-domain waveforms. The test is performed on 55 VGBs cataloged in Ref. [61]. Four distinct lengths of segments are considered: 10 days (grey), 5 days (yellow), 2.5 days (red), and 1 day (blue).

Further, the extended Whittle likelihood in terms of STFT reads

$$\ln \mathcal{L} = -\sum_{m=1}^{Nt}\sum_{n=1}^{N_{f.m}}\left[\frac{2}{T_m}\frac{|\bar{d}(t_m,f_n)-\bar{h}(t_m,f_n;\boldsymbol{\theta}_{\rm signal})|^2}{S(t_m,f_n;\boldsymbol{\theta}_{\rm noise})} + \ln S(t_m,f_n;\boldsymbol{\theta}_{\rm noise})\right]. \quad (33)$$

III. GB PARAMETER ESTIMATION

As a key component of LISA's prototype global analysis pipelines [25–27,91], FASTGB [81] is currently the state-of-the-art algorithm for rapid GB signal calculation in the frequency domain. In this work, we utilize its GPU implementation GBGPU [92–94] as a benchmark for the conventional frequency-domain analysis. Notice that the original GBGPU is based on LISA's equal-arm analytic orbit and first-generation TDI. To stay consistent with our interested scenario, we further adapt it to fit Taiji's numerical orbit and second-generation TDI. The adapted version can be found in public GitHub repository TRIANGLE-GB [95], and its validation against rigorous time-domain simulation is presented in the Appendix of Ref. [19].

Realistic space-based GW data analysis is featured by the need to simultaneously analyze and update the models of signals and noises. To emulate this situation without actually performing a costly global analysis, we designed a "noise-agnostic" workflow (distinguished from those that assume noise spectra are known), and implemented it in both frequency domain and time-frequency domain. This enables the comparison of their performances in the presence of nonstationary noises.

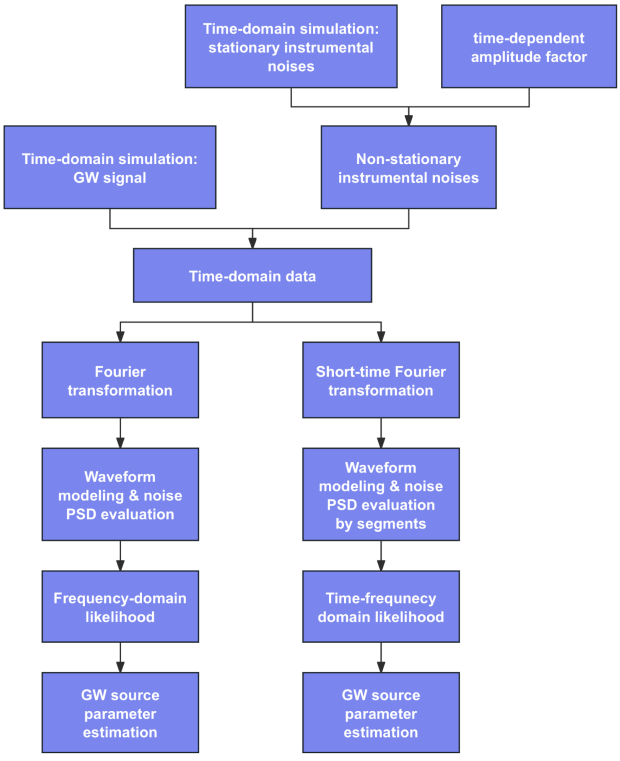

FIG. 2. "Noise agnostic" workflow.

As outlined in Fig. 2, we first simulate signals and noises separately in the form of second-generation TDI variables $\{A_2, E_2, T_2\}$ via TRIANGLE-SIMULATOR. For the estimation of GB parameters, only the quasiorthogonal "signal" channels A_2 and E_2 are considered. Simulating signals and noises separately enables the introduction of time varying noise amplitude before combination. Following the treatment of Ref. [32] (but applying to time dependence rather than frequency dependence), we let the noise spectrum vary by ± 1 order of magnitude relative to the average level. Cubic spline interpolation with 1 knot per month is adopted to model a generic slow-varying noise, and the knots for A_2, E_2 channels are generated independently. For each TDI channel, 13 knots are used for the 12-month data. Subsequently, the noises are further rescaled to ensure their averaged spectra over a year align with Taiji's nominal PSDs, hence guaranteeing the signal's signal-to-noise ratios (SNRs) are as expected.

When working in the frequency domain, a 10 μHz band centered at the initial frequency f_0 of the target signal is

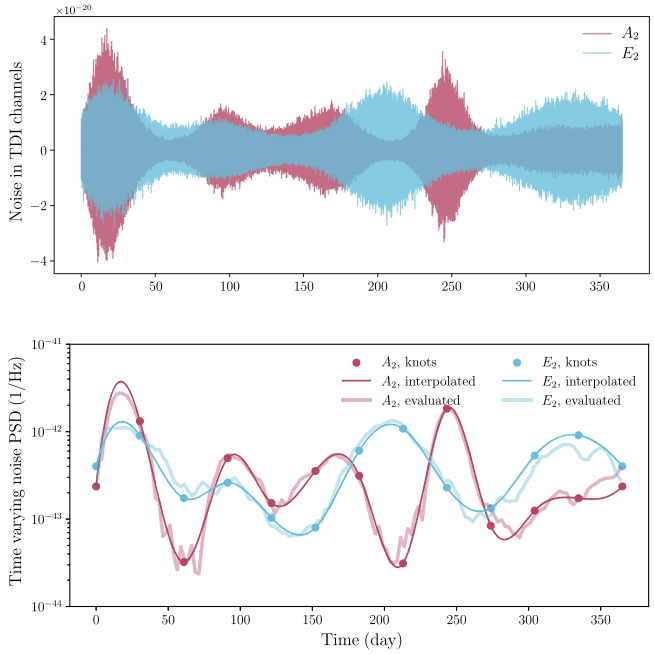

FIG. 3. Time-varying instrumental noises in the TDI-A_2, E_2 channels (upper panel), obtained by multiplying time-dependent amplitude factors (lower panel) to the original Gaussian stationary noises simulated with TRIANGLE-SIMULATOR. The amplitude factors, designed to mimic monthly variations, are generated by interpolating from 13 knots using cubic splines. Also shown in the lower panel are the time-varying noise PSDs evaluated following the median-smooth procedure, which will serve as a key element of the likelihood function.

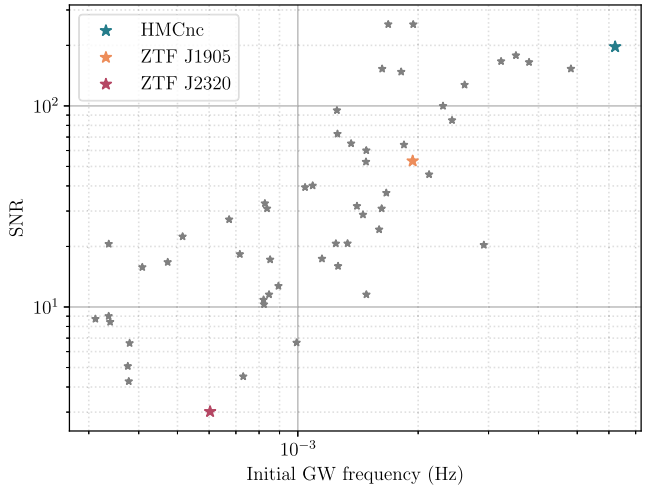

FIG. 4. SNR-f_0 plot for the tested 55 sources. Three of them (HMCnc, ZTF J1905, and ZTF J2320) are used as representative examples for the high-frequency, mid-low-frequency, and low-SNR sources in subsequent analysis.

used for analysis. This bandwidth is a conservative choice to ensure the entire evolution of the signal is accounted for. Evaluating noise PSD in the frequency domain is straightforward: we calculate the periodogram within this band and take the median values to avoid the disruption caused by signal [91,96] (neglecting the spectral shape due to the narrow bandwidth). On the other hand, in time-frequency domain, to capture the time dependence of PSD [i.e., to get $S(t, f_0)$], we select 50 μHz around f_0 (for the relatively coarse frequency resolution, also conservatively), calculate the median over this frequency band for each time segment, and further smooth the resulting $S(t, f_0)$ time series with the Savitzky-Golay filter [97] (see Fig. 3 for an example). One should notice that the uniform bin widths adopted in our work only serve as an *ad hoc* solution for VGBs. When applying our framework to GBs in broader frequency ranges, adaptive binning approaches, such as the method proposed in Ref. [98], should be prioritized.

Given the noise spectra, one can neglect all the $\boldsymbol{\theta}_{\rm noise}$ in Eq. (33), thus only the first line remains. For each TDI channel,

$$\ln \mathcal{L} = -\sum_{mn} \frac{2}{T_m} \frac{|\bar{d}(t_m, f_n) - \bar{h}(t_m, f_n; \boldsymbol{\theta}_{\rm signal})|^2}{S(t_m, f_n)}, \quad (34)$$

and the total log likelihood is obtained by summing over A_2 and E_2. Neglecting the dependence on t, the above expression reduces to the conventional frequency-domain formula used for comparison, where the term "conventional" suggests that correlations among different frequencies are not accounted for.

Tests are conducted on 55 VGBs following the "noise agnostic" workflow. For each VGB, both the noise realization and amplitude knots are regenerated. Notice that

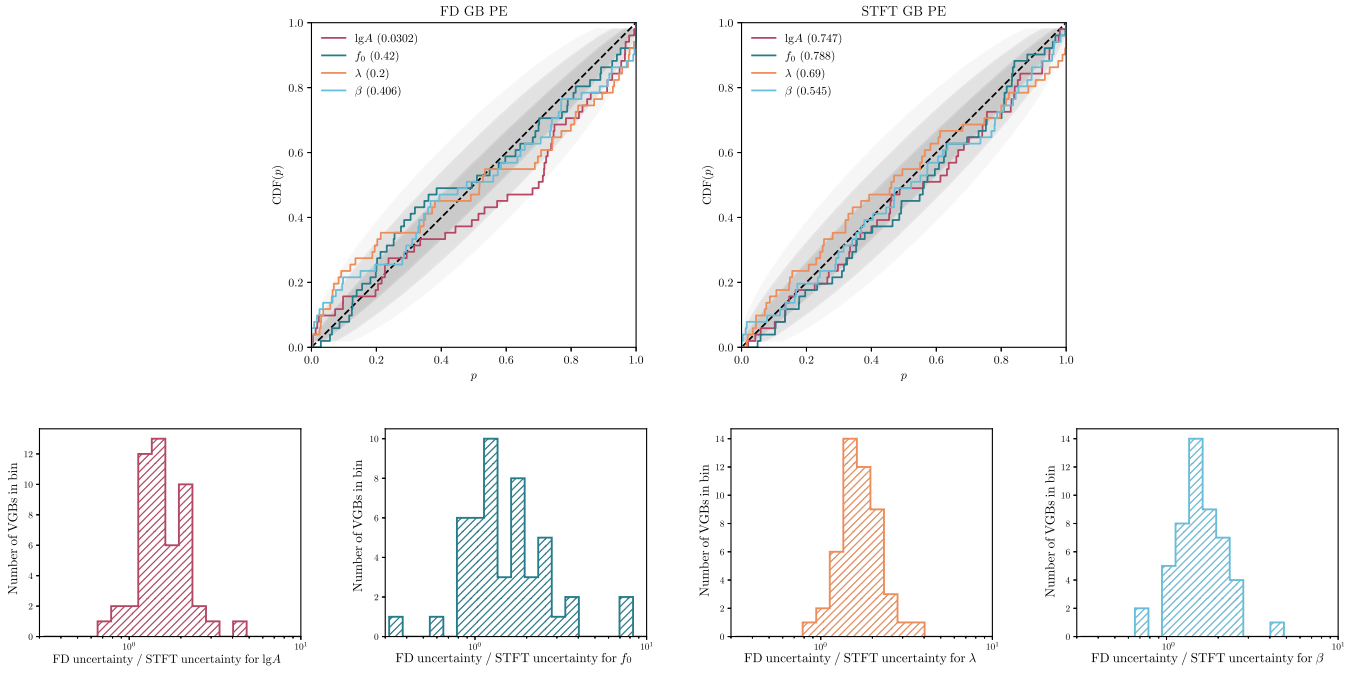

FIG. 5. Statistical summaries for four key parameters (amplitude A, initial frequency f_0, ecliptic longitude λ, and latitude β). The upper panels display the P-P plots for their posterior distributions based on frequency-domain and STFT parameter estimations. For each parameter, the curve represents the cumulative distribution function of the percentile scores of the true values. The black dashed line indicates ideal unbiased estimate, while gray regions denote the 1σ to 3σ confidence bounds. The p values of Kolmogorov-Smirnov test are provided in the legend. Compared in the lower panels are the uncertainties (i.e., 1σ credible interval widths) of parameters.

these VGBs are defined according to their detectability under 48-month observations [61], whereas the time span of our simulation is only 1 year. To ensure sufficient SNR for each source, the amplitudes of the first 25 sources (ordered per Ref. [99]) are amplified by a factor of 2, and the remaining 30 by a factor of 4. Figure 4 shows the SNR–f_0 diagram for the 55 tested sources. Markov Chain Monte Carlo (MCMC) sampling of the likelihood is conducted via the ERYN sampler [100] with affine invariant move, and the hyperparameters are set as N_WALKER=200, N_TEMPERATURE=4.

For instance, Appendix B displays the posterior distributions for two VGBs: one is HMCnc at high frequency ($f_0 = 6.22$ mHz, Fig. 10), and the other is ZTF J1905 at mid-low frequency ($f_0 = 1.94$ mHz, Fig. 11). The posteriors drawn from frequency-domain and STFT likelihoods are visualized in green and orange corner plots, respectively. These results preliminarily demonstrate the advantage of time-frequency analysis under nonstationary noise, as evidenced by reduced uncertainties and biases. Extending to more comprehensive comparison across all sources, Fig. 5 presents the statistical summaries of four key parameters (amplitude A, initial frequency f_0, ecliptic longitude λ, and latitude β) [101]. To compare the statistical unbiasedness of the two methods, the P-P plots for their posterior distributions are shown in the upper panels of Fig. 5. Evidently, both methods yield statistically unbiased results within the 3σ level, while the performance of the STFT approach is marginally superior across all the parameters of interest. Beyond unbiasedness tests, we further compare the parameter constraint capabilities of both methods by computing the ratio of their uncertainties (i.e., 1σ credible interval widths). Results are shown in the lower panels of FIG. 5. These comparisons confirm and generalize our previous conclusion drawn from HMCnc and ZTF J1905: under nonstationary noise, the STFT approach generally yields more tightly constrained source parameters. Additionally, an extreme case (ZTF J2320, Fig. 6) reveals that frequency-domain analysis may fail to detect relatively low-SNR [102] signals (SNR $= 3$) under nonstationary noise (the signal is almost "lost"), while it is successfully identified by STFT. This underscores that adopting appropriate data representations helps to ensures faithful characterization of detectability.

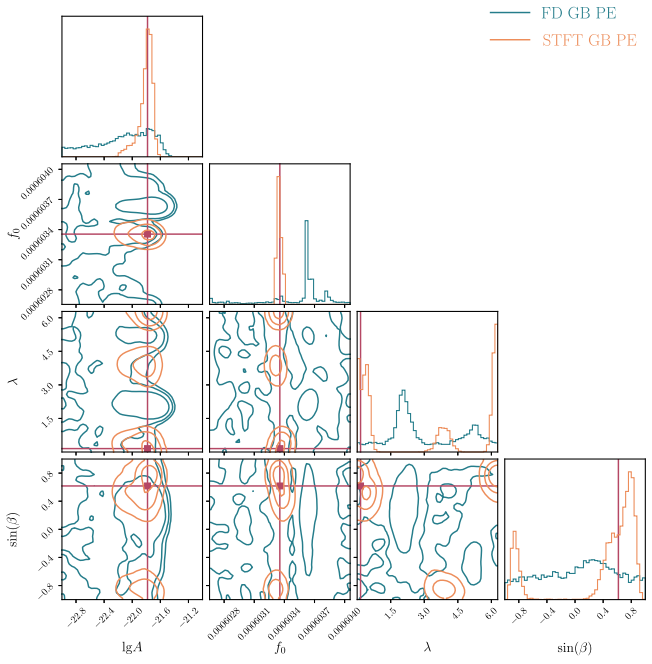

FIG. 6. Posteriors of VGB ZTF J2320 (SNR $= 3$) as an extreme example for the advantage of STFT analysis (orange) over frequnecy-domain analysis (green) under noise nonstationarity.

IV. INSTRUMENTAL NOISE CHARACTERIZATION

Accurate and comprehensive knowledge on instrumental noises is crucial for assessing the detector's operation status, as well as detecting resolvable and stochastic signals. Among all the configurations for TDI, the so called "null" channels are particularly significant for this purpose, because they are insensitive to GWs and mainly carry information about instrumental noises [38–40,103]. Within the widely adopted Michelson-type TDI channels, the T channel represents such a null configuration [38]. However, its effectiveness as a null channel is hindered by two factors. Firstly, for realistic unequal-armlength orbits, the T channel has comparable sensitivity with the signal channels at frequencies below 1 mHz and above 0.1 Hz [29,36,51]. Secondly, even ideally assuming the spectra $S_{ij,\mathrm{OMS}}$ and $S_{ij,\mathrm{ACC}}$ remain invariant through the whole mission lifetime, the resulting S_{T_2} for T channel still exhibits significant temporal instability since it is sensitive to armlength variations, making noise estimation in the frequency domain infeasible [52]. Regarding the first limitation, although the T channel is not perfectly immune to signals, its reduced sensitivity still permits early-stage decoupling from the global analysis, namely it can be used as a noise monitor after the few brightest signals have been subtracted. The second one is the main focus of this subsection. We demonstrate that, given the well-measured armlengths (to nanosecond precision [70,71]) and clearly known transfer functions form $S_{ij,\mathrm{OMS}}$ and $S_{ij,\mathrm{ACC}}$ to S_{T_2}, the time variation of S induced by armlength can be actually well modeled, hence enabling noise estimation in the time-frequency domain. Crucially, incorporating these modeled temporal information further relieves degeneracies among the noise parameters.

To focus on the effects of armlength variation, we first make some conventional simplifications as in previous studies (e.g., Refs. [26,28,29,35,40,52]): The spectral shapes of S_{OMS} and S_{ACC} are known and identical across all $ij \in \{12, 23, 31, 21, 32, 13\}$ [following Eq. (17)]. Only their amplitudes $A_{ij,\mathrm{OMS}}$ and $A_{ij,\mathrm{ACC,ij}}$ are to be estimated from

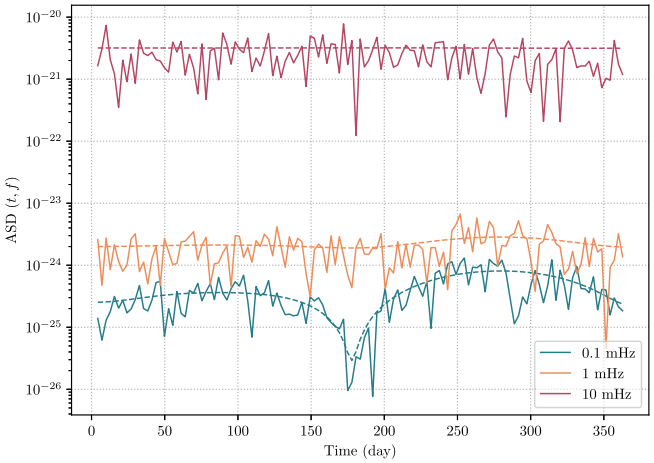

FIG. 7. Comparison between the T channel's noise model (dashed curves) and simulated data (solid curves) at three representative frequencies $\{0.1\ \text{mHz}, 1\ \text{mHz}, 10\ \text{mHz}\}$.

data, resulting in $6\times 2=12$ parameters $\boldsymbol{\theta}_{\text{noise}}=\{A_{ij,\text{OMS}}, A_{ij,\text{ACC}}\}$. Furthermore, $S_{ij,\text{ACC}}$ and $S_{ij,\text{OMS}}$ are assumed constant throughout the mission lifetime, thereby attributing all time dependence of S_{T_2} to armlength variation. Notably, the noises in realistic detection scenarios are surely more complicated, thus more flexible spectral modeling such as splines [36,104] or Gaussian processes [105] remain topics for future research.

The variations in the armlengths of Taiji exhibit monthly to yearly timescales, primarily due to orbital perturbations driven by celestial bodies in the Solar System [19,106–108]. Therefore, for the 2.5-day segmentation selected in Sec. II B, we can safely employ the time-frequency domain noise models of Eq. (29) and likelihood function of Eq. (33) under the local stationarity condition. For later convenience, we rewrite the PSD of T_2 channel as

$$S_{T_2}(t,f;\boldsymbol{\theta}_{\text{noise}})=\sum_{ij,\alpha}A^2_{ij,\alpha}F_{ij,\alpha}(t,f), \tag{35}$$

where $\alpha\in\{\text{OMS},\text{ACC}\}$. The time-frequency dependent contributors $F_{ij,\alpha}$ are calculated from the delay operators.

In Fig. 7, we select three representative frequencies $\{0.1\ \text{mHz}, 1\ \text{mHz}, 10\ \text{mHz}\}$ to compare the noise model of Eq. (35) with the time-varying PSD calculated from the time-domain simulations of TRIANGLE-SIMULATOR [we actually show the amplitude spectral densities (ASDs), defined as the square root of PSDs]. Besides verifying their consistency, the figure also shows that the time-dependence of $S_{T_2}(t,f)$ is particularly pronounced at low frequencies. Further, the time-frequency dependencies of $F_{ij,\text{OMS}}(t,f)$ and $F_{ij,\text{ACC}}(t,f)$ are plotted in the left six and right six subplots of Fig. 8, respectively. Most notably, the temporal pattern of $F_{ij,\text{ACC}}$ is distinguished across different ij. Given the functional form of Eq. (35), this feature will help to mitigate the degeneracies among parameters, especially $A_{ij,\text{ACC}}$.

Beyond providing a more rigorous theoretical foundation, we also perform MCMC search for noise parameters using the following noise-only likelihood,

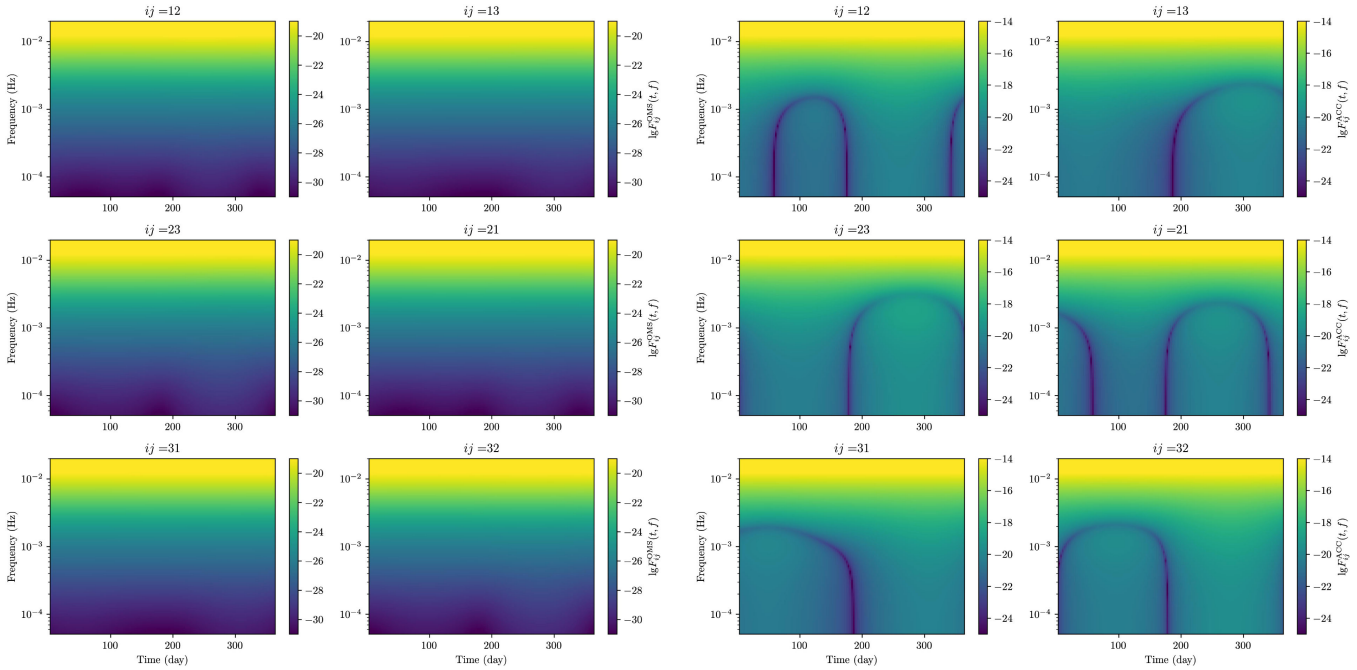

FIG. 8. Time-frequency dependence of contributors $F_{ij,\text{OMS}}$ (left six subplots) and $F_{ij,\text{ACC}}$ (right six subplots).

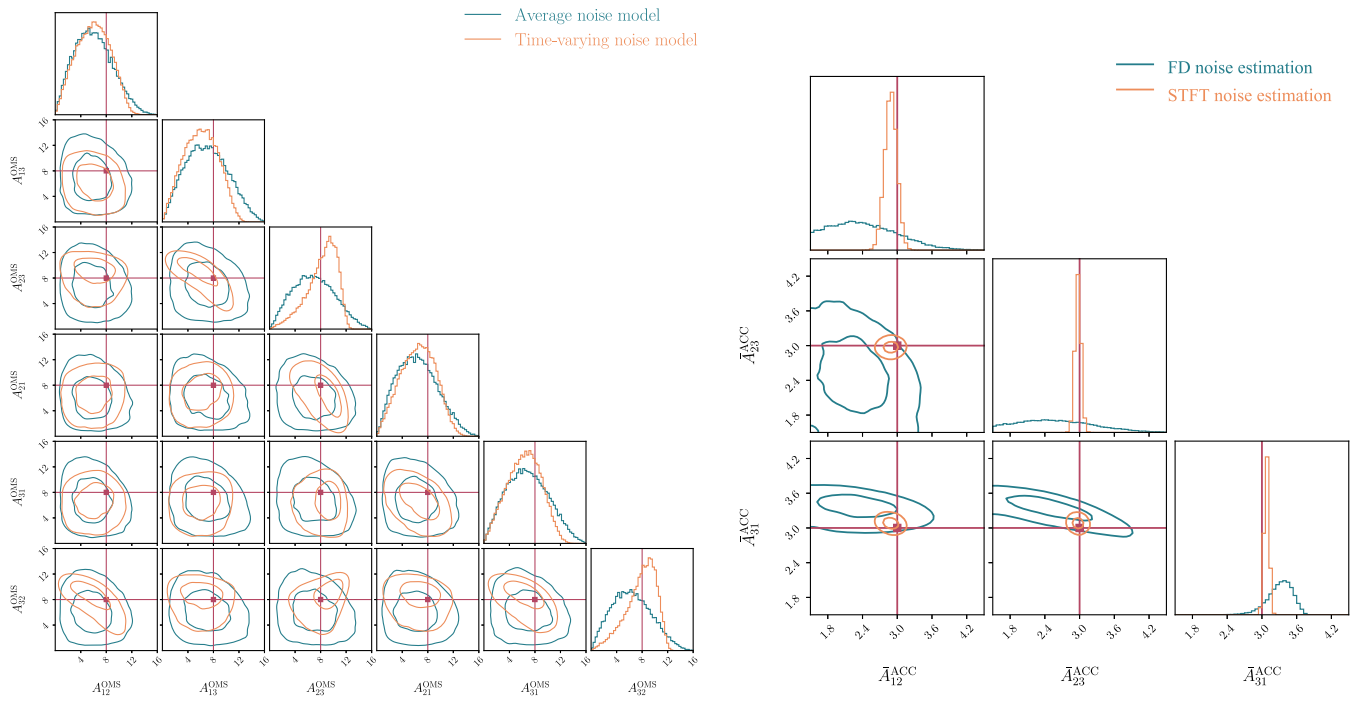

FIG. 9. Posterior distributions of OMS (left) and ACC (right) noise amplitudes. The ACC noise amplitudes are grouped pairwise as $\bar{A}_{ij,\mathrm{ACC}} \equiv \sqrt{(A^2_{ij,\mathrm{ACC}} + A^2_{ji,\mathrm{ACC}})/2}$.

$$\ln \mathcal{L} = -\sum_{mn} \left[\frac{2}{T_m} \frac{|\bar{d}(t_m, f_n)|^2}{S_{T_2}(t_m, f_n; \boldsymbol{\theta}_{\mathrm{noise}})} + \ln S_{T_2}(t_m, f_n; \boldsymbol{\theta}_{\mathrm{noise}}) \right]. \tag{36}$$

Notice that since $F_{ij,\alpha}$ are independent of the parameters, they can be precomputed before running MCMC (see the TDISENSITIVITY class of TRIANGLE-SIMULATOR for one implementation). As a result, each likelihood reduces to simple operations on known matrices. Besides, to avoid the oscillating behaviors near the "null" frequencies [109] ($\sim 0.025N$ Hz for Taiji, $N = 1, 2, 3, \ldots$), only the frequency range 5×10^{-5}—2×10^{-2} Hz is used. By neglecting the time dependence, the above expression reduces to the frequency-domain version. For frequency-domain estimation, we set the model for $S_{T_2}(f)$ as $S_{T_2}(t, f)$ averaged over the whole year. The configurations for the MCMC sampler and hyperparameters stay the same as Sec. III. In line with the conventions of Refs. [52,110], we present the posterior distributions of OMS and ACC noise amplitudes separately, and the ACC noise amplitudes are grouped pairwise as $\bar{A}_{ij,\mathrm{ACC}} \equiv \sqrt{(A^2_{ij,\mathrm{ACC}} + A^2_{ji,\mathrm{ACC}})/2}$ due to the strong intrapair correlations (i.e., ij vs ji. See the explanation in Ref. [52], and the sub-mHz section of $F_{ij,\mathrm{ACC}}$ in Fig. 8). Figure 9 compares the results of frequency-domain (green) and STFT (orange) analysis, with left and right panels showing the posterior distributions of $\bar{A}_{ij,\mathrm{ACC}}$ and $A_{ij,\mathrm{OMS}}$, respectively. Consistent with our theoretical predictions, by moving to time-frequency domain, the incorporation of modeled temporal features significantly mitigates the degeneracies among the ACC noise parameters, resulting in substantially improved constraints. For OMS noise parameters, a modest reduction in the uncertainty is also observed.

V. CONCLUSION AND OUTLOOK

This work develops a STFT-based Bayesian framework to address nonstationary noise in the long-duration GW data analysis of Taiji. Focusing on two significant tasks—GB parameter estimation and instrumental noise characterization—we derive GB waveform templates and time-varying noise spectral models, and further extend Bayesian inference statistics to the STFT domain. Compared with conventional frequency-domain methods, our framework demonstrates significantly enhanced accuracy and reduced bias of parameters, confirming the potential of time-frequency representations for the future analysis of realistic Taiji data.

Despite these advantages, certain limitations of the current work warrant further investigation:

Firstly, while the test on 55 individual VGBs confirms the advantages of our method, signal overlap remains the core challenge for Taiji data analysis, requiring integrating the time-frequency framework into the whole global analysis pipeline. The relatively sparse frequency resolution of STFT

may exacerbate the overlap of GB signals, hence increasing algorithmic complexity and computational demands. Nevertheless, results in Sec. III highlight STFT's critical role in improving the constraints on source parameters. Moreover, its more rigorous theoretical foundation under noise nonstationarity also ensures the interpretability and credibility of further scientific implications. Computationally, our CUPY-accelerated implementation achieves $\sim 10^4$ likelihood evaluations per second on a NVIDIA V100 GPU, showing potential scalability for more intensive calls by the global fit pipeline. Of course, before proceeding to global analysis, further tests on more extended source parameters and optimization in terms of efficiency and robustness are still required. Especially, although our derivation of the time-frequency domain model does not rely on the assumption of uniform T_m, its implementation must also be extended to the case of nonuniform T_m, in order to accommodate more realistic scenarios.

Secondly, our noise characterization with T channel assumes nonstationarity arises solely from armlength variations. Future work will incorporate the intrinsic drifts of instrumental noise components (OMS and ACC noises, etc). Besides, realistic detection would involve more complex or unknown noise spectral profiles, necessitating more flexible representations such as splines [36,111,112] and Gaussian process [105].

ACKNOWLEDGMENTS

This work is supported by the National Key Research and Development Program of China (Grants No. 2021YFC2201903, No. 2024YFC2207300, No. 2021YFC2201901, and No. 2020YFC2200100). We gratefully acknowledge He Wang at University of Chinese Academy of Sciences and Shichao Wu at Max-Planck-Institut für Gravitationsphysik for invaluable discussions and suggestions.

DATA AVAILABILITY

The data that support the findings of this article are not publicly available. The data are available from the authors upon reasonable request.

APPENDIX A: TUKEY WINDOW IN THE TIME AND FREQUENCY DOMAIN

For a Tukey window specified by parameter $\alpha \in [0, 1]$, its time-domain expression reads

$$w_T(t) = \begin{cases} \frac{1}{2} - \frac{1}{2}\cos\left[\frac{2\pi(t+T/2)}{\alpha T}\right], & -\frac{T}{2} \le t < \frac{\alpha-1}{2}T \\ 1, & \frac{\alpha-1}{2}T \le t < \frac{1-\alpha}{2}T \\ \frac{1}{2} - \frac{1}{2}\cos\left[\frac{2\pi(T/2-t)}{\alpha T}\right], & \frac{1-\alpha}{2}T \le t \le \frac{T}{2} \end{cases}. \tag{A1}$$

Applying Fthe ourier transform yields its frequency-domain representation,

$$\tilde{w}_T(f) = \frac{iA^{-1}(2B + A - 1) - iC^2[1 + A(2B - 1)]}{4\pi C(B - 1)f} + \frac{i(A^2C^2 - 1)}{2\pi ACf}, \tag{A2}$$

where we have defined

$$A \equiv e^{i\pi\alpha Tf}, \qquad B \equiv \alpha^2 T^2 f^2, \qquad C \equiv e^{-i\pi Tf}. \tag{A3}$$

APPENDIX B: THE FULL POSTERIORS OF VGB PARAMETERS BASED ON FREQUENCY-DOMAIN AND STFT ANALYSES

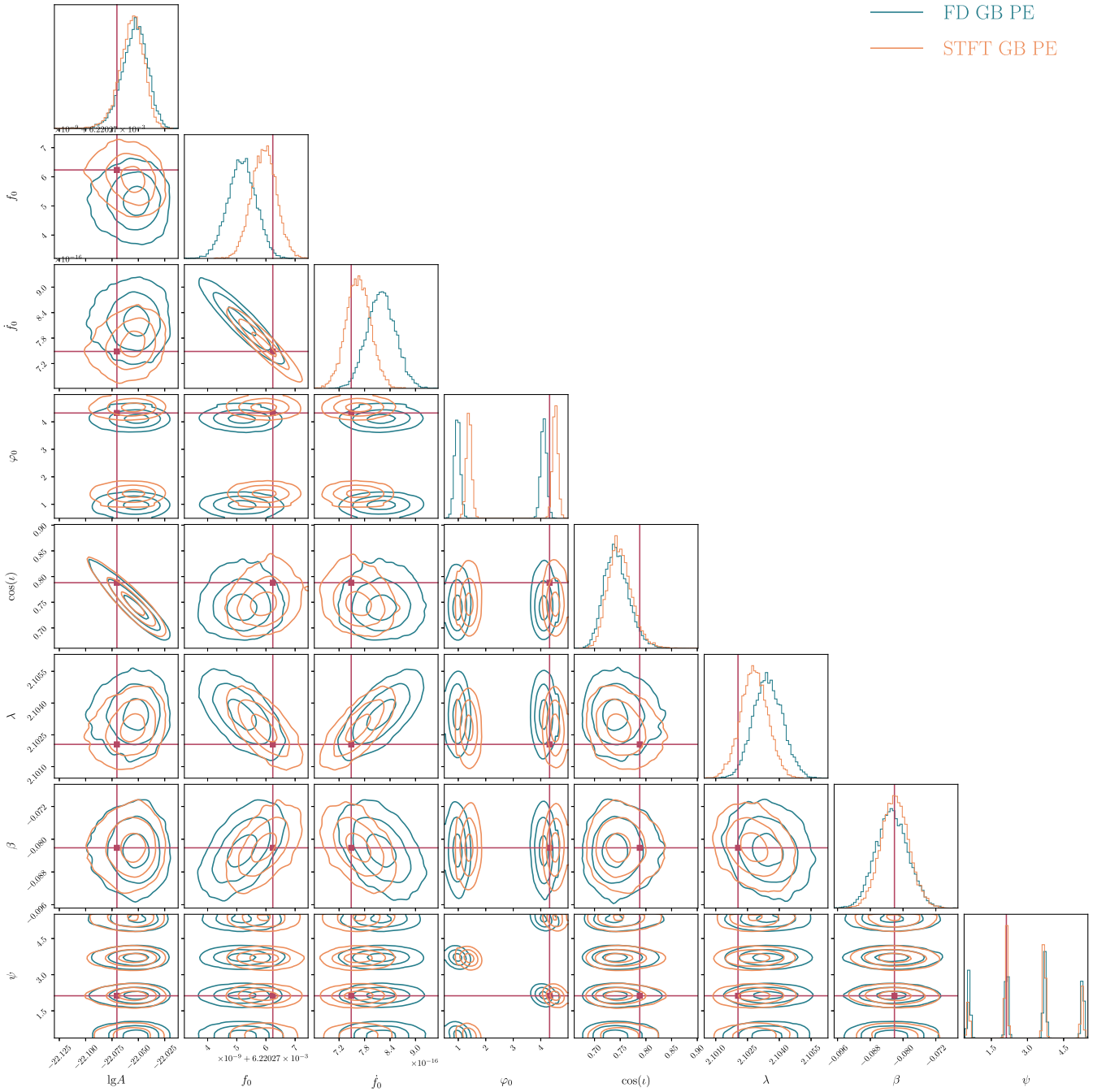

FIG. 10. Posterior distributions of high-frequency source HMCnc ($f_0 = 6.22$ mHz, SNR $= 197$) drawn from frequency-domain (green) and STFT (orange) likelihoods, respectively.

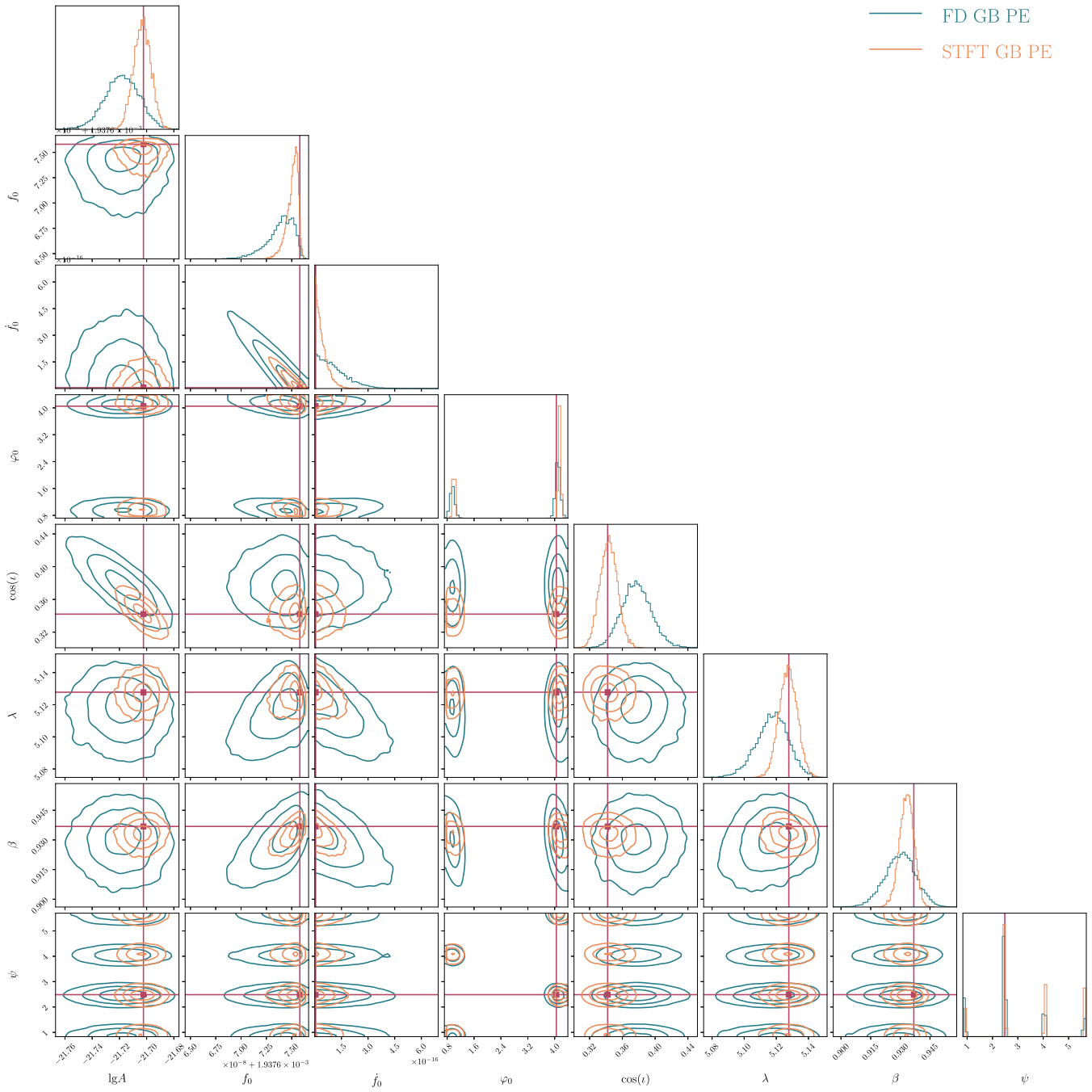

FIG. 11. Similar to Fig. 10, but for a mid-low-frequency source ZTF J1905 ($f_0 = 1.94$ mHz, SNR $= 53$).

[1] P. Amaro-Seoane, H. Audley, S. Babak, J. Baker, E. Barausse *et al.*, arXiv:1702.00786.
[2] J. Baker *et al.*, arXiv:1907.06482.
[3] W.-R. Hu and Y.-L. Wu, Natl. Sci. Rev. **4**, 685 (2017).
[4] Z. Luo, Z. Guo, G. Jin, Y. Wu, and W. Hu, Results Phys. **16**, 102918 (2020).
[5] Z. Luo, Y. Wang, Y. Wu, W. Hu, and G. Jin, Prog. Theor. Exp. Phys. **2021**, 05A108 (2020).

[6] J. Luo *et al.* (TianQin Collaboration), Classical Quantum Gravity **33**, 035010 (2016).
[7] K. Li, T. Bogdanović, D. R. Ballantyne, and M. Bonetti, Astrophys. J. **933**, 104 (2022).
[8] K. Li, T. Bogdanović, D. R. Ballantyne, and M. Bonetti, Astrophys. J. **959**, 3 (2023).
[9] N. Steinle, H. Middleton, C. J. Moore, S. Chen, A. Klein, G. Pratten, R. Buscicchio, E. Finch, and A. Vecchio, Mon. Not. R. Astron. Soc. **525**, 2851 (2023).
[10] A. Lamberts, S. Blunt, T. B. Littenberg, S. Garrison-Kimmel, T. Kupfer, and R. E. Sanderson, Mon. Not. R. Astron. Soc. **490**, 5888 (2019).
[11] V. Korol, E. M. Rossi, P. J. Groot, G. Nelemans, S. Toonen, and A. G. A. Brown, Mon. Not. R. Astron. Soc. **470**, 1894 (2017).
[12] V. Korol, N. Hallakoun, S. Toonen, and N. Karnesis, Mon. Not. R. Astron. Soc. **511**, 5936 (2022).
[13] M. Benacquista, Lisa and the galactic population of compact binaries, in *Handbook of Gravitational Wave Astronomy*, edited by C. Bambi, S. Katsanevas, and K. D. Kokkotas (Springer Singapore, Singapore, 2020), pp. 1–24.
[14] J. R. Gair, L. Barack, T. Creighton, C. Cutler, S. L. Larson, E. S. Phinney, and M. Vallisneri, Classical Quantum Gravity **21**, S1595 (2004).
[15] J. Chen, C.-S. Yan, Y.-J. Lu, Y.-T. Zhao, and J.-Q. Ge, Res. Astron. Astrophys. **21**, 285 (2021).
[16] R. Buscicchio, J. Torrado, C. Caprini, G. Nardini, N. Karnesis, M. Pieroni, and A. Sesana, J. Cosmol. Astropart. Phys. 01 (2025) 084.
[17] S. Babak, C. Caprini, D. G. Figueroa, N. Karnesis, P. Marcoccia, G. Nardini, M. Pieroni, A. Ricciardone, A. Sesana, and J. Torrado, J. Cosmol. Astropart. Phys. 08 (2023) 034.
[18] C. Caprini *et al.*, J. Cosmol. Astropart. Phys. 03 (2020) 024.
[19] M. Du *et al.*, arXiv:2505.16500.
[20] K. Breivik, C. M. F. Mingarelli, and S. L. Larson, Astrophys. J. **901**, 4 (2020).
[21] R. Ebadi, V. Strokov, E. H. Tanin, E. Berti, and R. L. Walsworth, Phys. Rev. D **111**, 044023 (2025).
[22] C. Liu, W.-H. Ruan, and Z.-K. Guo, Phys. Rev. D **107**, 064021 (2023).
[23] N. Karnesis, S. Babak, M. Pieroni, N. Cornish, and T. Littenberg, Phys. Rev. D **104**, 043019 (2021).
[24] T. Littenberg, N. Cornish, K. Lackeos, and T. Robson, Phys. Rev. D **101**, 123021 (2020).
[25] T. B. Littenberg and N. J. Cornish, Phys. Rev. D **107**, 063004 (2023).
[26] M. L. Katz, N. Karnesis, N. Korsakova, J. R. Gair, and N. Stergioulas, Phys. Rev. D **111**, 024060 (2025).
[27] S. Deng, S. Babak, M. Le Jeune, S. Marsat, E. Plagnol, and A. Sartirana, Phys. Rev. D **111**, 103014 (2025).
[28] G. Wang, B. Li, P. Xu, and X. Fan, Phys. Rev. D **106**, 044054 (2022).
[29] O. Hartwig, M. Lilley, M. Muratore, and M. Pieroni, Phys. Rev. D **107**, 123531 (2023).
[30] M. H. A. Davis, *Gravitational Wave Data Analysis* (Springer, Netherlands, 1989).
[31] P. Jaranowski and A. Krolak, *Analysis of Gravitational-Wave Data*, Cambridge Monographs on Particle Physics, Nuclear Physics and Cosmology (Cambridge University Press, Cambridge, England, 2009).
[32] M. Muratore, J. Gair, and L. Speri, Phys. Rev. D **109**, 042001 (2024).
[33] C. Caprini, D. G. Figueroa, R. Flauger, G. Nardini, M. Peloso *et al.*, J. Cosmol. Astropart. Phys. 11 (2019) 017.
[34] R. Flauger, N. Karnesis, G. Nardini, M. Pieroni, A. Ricciardone, and J. Torrado, J. Cosmol. Astropart. Phys. 01 (2021) 059.
[35] G. Boileau, N. Christensen, R. Meyer, and N. J. Cornish, Phys. Rev. D **103**, 103529 (2021).
[36] Q. Baghi, N. Karnesis, J.-B. Bayle, M. Besançon, and H. Inchauspé, J. Cosmol. Astropart. Phys. 04 (2023) 066.
[37] M. Tinto and S. Dhurandhar, Living Rev. Relativity **24**, 1 (2021).
[38] M. Muratore, D. Vetrugno, S. Vitale, and O. Hartwig, Phys. Rev. D **105**, 023009 (2022).
[39] O. Hartwig and M. Muratore, Phys. Rev. D **105**, 062006 (2022).
[40] M. Muratore, O. Hartwig, D. Vetrugno, S. Vitale, and W. J. Weber, Phys. Rev. D **107**, 082004 (2023).
[41] P.-P. Wang, X.-Y. Lu, X.-L. Zhao, H.-K. Chen, J. Zhou, W. Huang, Y.-J. Tan, H.-Z. Wu, and C.-G. Shao, Results Phys. **58**, 107481 (2024).
[42] The focus of this paper primarily lies in slowly drifting noises. Transient noises such as glitches can be addressed with alternative methods like fitting and subtraction [43,44].
[43] M. Muratore, J. Gair, O. Hartwig, M. L. Katz, and A. Toubiana, Phys. Rev. D **112**, 063041 (2025).
[44] Q. Baghi, N. Korsakova, J. Slutsky, E. Castelli, N. Karnesis, and J.-B. Bayle, Phys. Rev. D **105**, 042002 (2022).
[45] M. R. Adams and N. J. Cornish, Phys. Rev. D **89**, 022001 (2014).
[46] S. Lin, B. Hu, X.-H. Zhang, and Y.-X. Liu, Sci. China Phys. Mech. Astron. **66**, 299512 (2023).
[47] F. Pozzoli, R. Buscicchio, A. Klein, V. Korol, A. Sesana , and F. Haardt, Phys. Rev. D **111**, 063005 (2025).
[48] M. Armano, H. Audley, G. Auger, J. T. Baird, M. Bassan *et al.*, Phys. Rev. Lett. **116**, 231101 (2016).
[49] M. Armano, H. Audley, J. Baird, P. Binetruy, M. Born *et al.*, Phys. Rev. D **97**, 122002 (2018).
[50] M. Armano, H. Audley, J. Baird, P. Binetruy, M. Born *et al.*, Phys. Rev. Lett. **120**, 061101 (2018).
[51] G. Wang and W.-T. Ni, Phys. Scr. **98**, 075005 (2023).
[52] G. Wang, Phys. Rev. D **110**, 064085 (2024).
[53] P. Whittle, J. R. Stat. Soc. Ser. B **19**, 38 (1957).
[54] Q. Baghi, I. Thorpe, J. Slutsky, J. Baker, T. Dal Canton, N. Korsakova, and N. Karnesis, Phys. Rev. D **100**, 022003 (2019).
[55] N. J. Cornish, Phys. Rev. D **102**, 124038 (2020).
[56] M. C. Digman and N. J. Cornish, Astrophys. J. **940**, 10 (2022).
[57] M. C. Digman and N. J. Cornish, Phys. Rev. D **108**, 023022 (2023).
[58] R. Tenorio and D. Gerosa, Phys. Rev. D **111**, 104044 (2025).
[59] S. Kumar, A. H. Nitz, and X. J. Forteza, Astrophys. J. **982**, 67 (2025).

[60] S. Klimenko, I. Yakushin, A. Mercer, and G. Mitselmakher, Classical Quantum Gravity **25**, 114029 (2008).
[61] T. Kupfer *et al.*, Astrophys. J. **963**, 100 (2024).
[62] A. W. Criswell, S. Rieck, and V. Mandic, Phys. Rev. D **111**, 023025 (2025).
[63] M. Otto, Time-delay interferometry simulations for the Laser Interferometer Space Antenna, Ph.D. thesis, Leibniz University, Hannover, 2015.
[64] O. Hartwig, Instrumental modelling and noise reduction algorithms for the Laser Interferometer Space Antenna, Ph.D. thesis, Leibniz University, Hannover, 2021.
[65] J.-B. Bayle and O. Hartwig, Phys. Rev. D **107**, 083019 (2023).
[66] P. Wu, M. Du, and P. Xu, Opt. Express **32**, 43249 (2024).
[67] M. L. Katz, J.-B. Bayle, A. J. K. Chua, and M. Vallisneri, Phys. Rev. D **106**, 103001 (2022).
[68] L. WG, LISA data challenge manual, https://sbgvm-151-90.in2p3.fr/static/data/pdf/LDC-manual-002.pdf.
[69] Z. Ren, T. Zhao, Z. Cao, Z.-K. Guo, W.-B. Han, H.-B. Jin, and Y.-L. Wu, Front. Phys. (Beijing)**18**, 64302 (2023).
[70] J. N. Reinhardt, M. Staab, K. Yamamoto, J.-B. Bayle, A. Hees, O. Hartwig, K. Wiesner, S. Shah, and G. Heinzel, Phys. Rev. D **109**, 022004 (2024).
[71] J. N. Reinhardt, O. Hartwig, and G. Heinzel, Classical Quantum Gravity **42**, 055014 (2025).
[72] D. Quang Nam, Y. Lemière, A. Petiteau, J.-B. Bayle, O. Hartwig, and M. Staab, Phys. Rev. D **108**, 082004 (2023).
[73] M. Tinto and S. Dhurandhar, Living Rev. Relativity **24**, 1 (2021).
[74] M. Tinto and S. V. Dhurandhar, Living Rev. Relativity **8**, 4 (2005).
[75] P.-P. Wang, W.-L. Qian, Y.-J. Tan, H.-Z. Wu, and C.-G. Shao, Phys. Rev. D **106**, 024003 (2022).
[76] T. A. Prince, M. Tinto, S. L. Larson, and J. W. Armstrong, Phys. Rev. D **66**, 122002 (2002).
[77] M. B. Priestley, J. R. Stat. Soc. Ser. B **27**, 204 (1965).
[78] O. Burke, S. Marsat, J. R. Gair, and M. L. Katz, Phys. Rev. D **111**, 124053 (2025).
[79] E. Castelli, Q. Baghi, J. G. Baker, J. Slutsky, J. Bobin, N. Karnesis, A. Petiteau, O. Sauter, P. Wass, and W. J. Weber, Classical Quantum Gravity **42**, 065018 (2025).
[80] P. A. Seoane *et al.*, Gen. Relativ. Gravit. **54**, 3 (2022).
[81] N. J. Cornish and T. B. Littenberg, Phys. Rev. D **76**, 083006 (2007).
[82] V. Korol, N. Hallakoun, S. Toonen, and N. Karnesis, Mon. Not. R. Astron. Soc. **511**, 5936 (2022).
[83] V. Korol, E. M. Rossi, P. J. Groot, G. Nelemans, S. Toonen, and A. G. A. Brown, Mon. Not. R. Astron. Soc. **470**, 1894 (2017).
[84] When modeling the TDI response of GB signal, the amplitude evolves slowly and can be calculated on a sparse time grid without loss of precision, leaving the accuracy of the phase as our primary focus. To set a criterion for the accuracy of the template, we require the residual SNR caused by template error to be less than 1. For an order-of-magnitude estimation, we assume a small constant phase error $\Delta\varphi$ and an original SNR ρ_0. It follows that the SNR of template error approximates $\Delta\varphi\rho_0$. Therefore, for the vast majority of observable GBs, $\Delta\varphi < 10^{-2}$ should suffice to meet the accuracy criterion. The threshold of $\Delta\varphi < 1/\rho$ is also commonly adopted in the literature on EMRI waveforms [85,86].
[85] T. Hinderer and E. E. Flanagan, Phys. Rev. D **78**, 064028 (2008).
[86] M. L. Katz, A. J. K. Chua, L. Speri, N. Warburton, and S. A. Hughes, Phys. Rev. D **104**, 064047 (2021).
[87] The difference between d_{ij} and d_{ji} is crucial for the suppression of laser noise, though.
[88] https://github.com/TriangleDataCenter/Triangle-Simulator.
[89] L. Lindblom, B. J. Owen, and D. A. Brown, Phys. Rev. D **78**, 124020 (2008).
[90] M. Pürrer and C.-J. Haster, Phys. Rev. Res. **2**, 023151 (2020).
[91] S. H. Strub, L. Ferraioli, C. Schmelzbach, S. C. Stähler, and D. Giardini, Phys. Rev. D **110**, 024005 (2024).
[92] M. L. Katz, C. Danielski, N. Karnesis, V. Korol, N. Tamanini, N. J. Cornish, and T. B. Littenberg, Mon. Not. R. Astron. Soc. **517**, 697 (2022).
[93] T. Robson, N. J. Cornish, N. Tamanini, and S. Toonen, Phys. Rev. D **98**, 064012 (2018).
[94] M. L. Katz, mikekatz04/gbgpu: First official public release! (2022).
[95] https://github.com/TriangleDataCenter/Triangle-GB.
[96] B. Allen, W. G. Anderson, P. R. Brady, D. A. Brown, and J. D. E. Creighton, Phys. Rev. D **85**, 122006 (2012).
[97] R. W. Schafer, IEEE Signal Process. Mag. **28**, 111 (2011).
[98] S. H. Strub, L. Ferraioli, C. Schmelzbach, S. C. Stähler, and D. Giardini, Phys. Rev. D **108**, 103018 (2023).
[99] LISA Collaboration, LISA Verification Binaries, https://gitlab.in2p3.fr/LISA/lisa-verification-binaries (2024).
[100] N. Karnesis, M. L. Katz, N. Korsakova, J. R. Gair, and N. Stergioulas, Mon. Not. R. Astron. Soc. **526**, 4814 (2023).
[101] For parameters with multimodal distributions (e.g., the sky locations of some sources), we employ SCIPY's FIND_PEAKS method to select only the peak with maximum likelihood values.
[102] Within the authors' knowledge, the specific SNR threshold for GB's detectability is yet to be established in the literature. For example, Refs. [23,61] adopted values of $5 \sim 7$. In our work, "low-SNR signals" refers to the signals that are near threshold or subthreshold.
[103] C. J. Hogan and P. L. Bender, Phys. Rev. D **64**, 062002 (2001).
[104] Y.-N. Li, Y.-M. Hu, and E.-K. Li, Classical Quantum Gravity **42**, 135003 (2025).
[105] F. Pozzoli, R. Buscicchio, C. J. Moore, F. Haardt, and A. Sesana, Phys. Rev. D **109**, 083029 (2024).
[106] G. Wang and W.-T. Ni, Res. Astron. Astrophys. **19**, 058 (2019).
[107] X. Han, X. Peng, W. Tang, Z. Yang, X. Ma *et al.*, Phys. Rev. D **106**, 102005 (2022).
[108] Y.-Y. Zhang, G. Li, and B. Wen, Universe **10**, 219 (2024).
[109] G. Wang, Phys. Rev. D **110**, 042005 (2024).
[110] G. Wang, arXiv:2502.03983.
[111] Y.-N. Li, Y.-M. Hu, and E.-K. Li, Classical Quantum Gravity **42**, 135003 (2025).
[112] T. B. Littenberg and N. J. Cornish, Phys. Rev. D **91**, 084034 (2015).